JM PAPERS

Acoustically excited bubble tunnelling through soft material

Pratik Das[1] , **Ratnesh K. Shukla**[2] **and Jonathan B. Freund**[3]

[1]Department of Mechanical Engineering, Indian Institute of Technology Delhi, Hauz Khas, New Delhi, Delhi 110016, India

[2]Department of Mechanical Engineering, Indian Institute of Science, Bangalore 560012, India

[3]Department of Aerospace Engineering, University of Illinois Urbana–Champaign, Urbana, IL 61801, USA

Corresponding author: Pratik Das, pdas@mech.iitd.ac.in

Experiments have shown that ultrasound-stimulated microbubbles can translate through gel phantoms and tissues, leaving behind tunnel-like degraded regions. A computational model is used to examine the tunnelling mechanisms in a model material with well-defined properties. The high strain rates motivate the neglect of weak elasticity in favour of viscosity, which is taken to degrade above a strain threshold. The reference parameters are motivated by a 1 µm diameter bubble in a polysaccharide gel tissue phantom. This is a reduced model and data are scarce, so close quantitative agreement is not expected, but tunnels matching observations do form at realistic rates, which provides validation sufficient to analyse potential mechanisms. Simulations of up to 100 acoustic cycles are used to track tunnelling over 10 bubble diameters, including a steady tunnelling phase during which tunnels extend each forcing cycle in two steps: strain degrades the tunnel front during the bubble expansion, and then the bubble is drawn further along the tunnel during its subsequent inertial collapse. Bubble collapse jetting is damaging, though it is only observed during a transient for some initial conditions. There is a threshold behaviour when the viscosity of the undamaged material changes the character of the inertial bubble oscillation. Apart from that, the tunnel growth rate is relatively insensitive to the high viscosity of the material. Higher excitation amplitudes and lower frequencies accelerate tunnelling. That acoustic radiation force, elasticity and bubble jetting are not required is a principal conclusion.

Key words: biomedical flows, bubble dynamics, cavitation
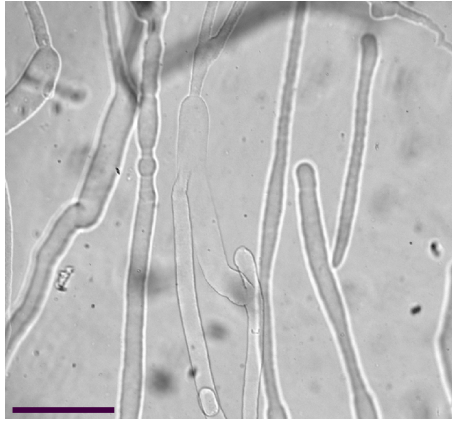
P. Das, R.K. Shukla and J.B. Freund

Figure 1. Microtunnels in soft agarose gel (Williams & Miller 2003). The scale bar indicates 500 μm.

1. Introduction

When exposed to ultrasound excitation, small bubbles in soft materials (e.g. viscoelastic gels, tissues and fibrous clots) have been observed to translate, leaving tunnels in their path (Williams & Miller 2003; Caskey *et al.* 2009*a*; Maxwell *et al.* 2010) (see example in figure 1). Driven bubble oscillations are thought to degrade material near the bubble, allowing it to travel through the material at nearly uniform speed (Caskey *et al.* 2009*a*; Acconcia *et al.* 2015). This travel leaves tunnel-like features (Williams & Miller 2003; Caskey *et al.* 2009*a*) of a width comparable to that expected for expanded bubbles (Caskey *et al.* 2009*a*). The mechanisms of this tunnelling are investigated here with simulations of model material.

Such tunnelling is potentially important in the mechanical disruption of tissue in histotripsy procedures (Maxwell *et al.* 2010; Kim *et al.* 2011; Lundt *et al.* 2017; Stride & Coussios 2019). In particular, Maxwell *et al.* (2010) observed bubble-scale tunnels in both high-intensity focused ultrasound (HIFU) treatment of an *ex vivo* kidney and in tissue-mimicking phantoms. They showed that tunnels formed by individual bubbles can overlap and create wide lesions. Similar tunnels were also seen in pre- and post-focus regions of HIFU treatment (Maxwell *et al.* 2010; Kim *et al.* 2011; Lundt *et al.* 2017). Kim *et al.* (2011) suggested that this collateral damage is caused by the activity of bubbles outside of the main targeted treatment zone. Lundt *et al.* (2017) also found tunnel-like features outside the HIFU treatment region, mostly in the post-focal tissue adjacent to the distal margin of the target.

Tunnelling has also been observed during ultrasound-accelerated thrombolysis by Acconcia *et al.* (2014), who saw individual ultrasound-excited microbubbles penetrate and transit clots, leaving a tunnel in their path. Acconcia *et al.* (2014) found that the penetration distance depends on the bubble size and the acoustic pressure. They hypothesised that both bubble oscillation and acoustic radiation forces on the bubbles might induce sufficient local strain to disrupt. Insonated microbubbles are also thought to enhance extravascular drug delivery by penetrating otherwise impermeable tissues and membranes, such as blood vessel walls or the blood–brain barrier, with tunnel-like features (Caskey *et al.* 2009*b*; Arvanitis *et al.* 2011; Stride & Coussios 2019).

Although it is clear that the driven bubbles somehow cause tunnelling, the details are hard to assess because it occurs internal to the material and is small scale (∼100 μm) and high frequency (∼MHz). Williams & Miller (2003) first observed the formation of tunnels

in a transparent agarose gel block immersed in water upon exposure to 4 MPa ultrasound delivered at 0.78 MHz (figure 1). They found tunnels in the gel sample that were open to the water bath, as well as fully within the gel. The number of tunnels increased with driving pressure amplitude, the duration of exposure to the ultrasound, and the dissolved gas content and cavitation nuclei. They postulated that bubbles burrowed through the gel, leaving a lower-viscosity fluid in their wake, with the tunnel diameters corresponding to the expected oscillation maximum of the excited bubbles. Williams & Miller (2003) found that the tunnels that initiated at the surface of the gel sample contained fluid with a lower viscosity compared with the tunnels that initiated within the gel. This degraded material behaved like a liquid more viscous than water. More recently, using high-speed microscopy, Caskey and collaborators (Caskey *et al.* 2009*a*,*b*) showed cavitation activity within a tissue-mimicking gel. High-speed microscopy images show asymmetric bubble oscillations near the growing end of the tunnel. Caskey *et al.* (2009*a*) found that bubble size in the expansion phase indeed approximately matched the tunnel diameter. The well-known jetting collapse of acoustically forced bubbles (Plesset & Chapman 1971; Popinet & Zaleski 2002; Johnsen & Colonius 2009; Ohl, Klaseboer & Khoo 2015; Krishnan, Hopfinger & Puthenveettil 2017; Zeng, An & Ohl 2022) was observed by Caskey *et al.* (2009*a*,*b*) during these asymmetric oscillations. However, these jets were not always oriented along the tunnel axis. Hence, their role in growing the tunnel in a particular direction is unclear. Still, a simple analysis based on an assumed jet velocity suggested that pressure on the gel at the jet impact might lead to strains that degrade the material.

It has also been recognised that material near the growing end is stretched during the expansion, which might also lead to degradation. This is the more consequential mechanism for the systems we consider, as will be seen in § 3. Caskey *et al.* (2009*a*) hypothesised that the tunnels form due to the combined effect of the bubble expansion and microjetting during collapse. However, diagnostic challenges and material complexity hinder direct assessment. In summary, the primary candidate mechanisms are collapse-induced bubble jetting, causing local high strains near the point of jet impact, or strain caused by large expansion of the bubble. The ultrasound wavelengths are much larger than the bubble size, so the pressure gradient across it is small, though it still exerts a net force on the bubble. This acoustic radiation force has been suggested as the mechanism that moves the bubble (or bubbles) along the tunnel, facilitating its growth (Caskey *et al.* 2009*a*,*b*; Acconcia *et al.* 2014; Stride & Coussios 2019). The present model (§ 2) does not include this force, but still produces tunnelling.

The goal of this study is to analyse, in greater detail than can be inferred from experiments, how a tunnel can grow in a model material, including how growth depends on the model parameters. Specifically, we introduce what is potentially the simplest possible scenario: a single acoustically excited insoluble gas bubble initialised near the end of a proto-tunnel within a viscous fluid material with viscosity that irreversibly drops with a fast time scale upon reaching a strain threshold. That this simple model reproduces observations is of importance itself, showing that the complexity of real material, elastic effects and acoustic radiation forces are not essential for tunnelling. This nominally axisymmetric configuration allows for simulations over hundreds of driving cycles to achieve seemingly asymptotic steady tunnelling. That it does reproduce tunnelling, as observed and at a reasonable tunnelling rate, provides sufficient validation for studying mechanisms even though no point-to-point comparison can be expected.

These simulations build, of course, on a history of simulation models: the symmetric bubble dynamics in an homogeneous medium (Plesset & Prosperetti 1977; Prosperetti & Lezzi 1986; Murakami *et al.* 2021) and the asymmetric jetting collapse of the bubbles near rigid walls (Popinet & Zaleski 2002; Huang & Zhang 2007; Johnsen & Colonius

2009; Rodriguez *et al.* 2022; Zeng *et al.* 2022; Li *et al.* 2023; Lang, Adami & Adams 2024). Studies of driven bubble dynamics near fluid–fluid interfaces do not consider steady tunnelling (Klaseboer & Khoo 2004; Freund, Shukla & Evan 2009; Orthaber *et al.* 2020; Yamamoto & Komarov 2020; Han *et al.* 2022).

Section 2 describes the configuration and the computational model. The simulation results are analysed in the sections that follow: the primary tunnelling mechanisms for this configuration are identified in § 3, followed by an assessment of the influence of the material properties in § 4, and acoustic excitation amplitude and frequency in § 5. The unexpected availability of multiple steady tunnelling conditions, for the same physical parameters arrived at from different initial conditions, is discussed in § 6. Finally, conclusions are summarised in § 7.

2. Simulation model

2.1. *Physical system*

The gas within the bubble is taken to be homogenous, inviscid and insoluble (Barajas & Johnsen 2017; Hasan *et al.* 2021). It is also assumed to be adiabatic due to the high frequencies ($\gtrsim 1\,\mathrm{MHz}$) of the driving ultrasound. Tissues and gels are nearly incompressible, which is enforced outside of the bubble. These same assumptions underly the Rayleigh–Plesset equation (Rayleigh 1917; Plesset 1949).

The material outside the bubble is a Newtonian fluid. Although this neglects the weak elasticity of gels and tissues, numerical studies have shown that the viscosity of similar materials has a stronger effect on the amplitude of fast microbubble oscillation than their elasticity (Yang & Church 2005; Freund 2008; Movahed *et al.* 2016; Murakami *et al.* 2021). This is further shown through a scaling analysis in § 2.2 for the baseline model parameters.

Tunnelling requires the degradation of the material. For this, we invoke the simplest tensorially consistent model based on a threshold for the maximum principal tensile strain. The effect of the degradation is to reduce the material's viscous resistance, the model for which is introduced in § 2.3.

2.2. *Configuration*

Some tunnels have been observed to bend and even fork (Williams & Miller 2003; Caskey *et al.* 2009*a*; Kim *et al.* 2011), but our focus is basic linear tunnelling, for which an axisymmetric model is sufficient. The initial configuration is shown in figure 2. The initial bubble with diameter $D_i = 1\,\mu\mathrm{m}$ starts centred at $(x, r) = (0, 0)$. The tunnel is initiated with the bubble at the end of a capsule-shaped low-viscosity (fully degraded) inclusion. This tunnel geometry is constructed for convenience, but simulations will run for sufficient numbers of cycles and tunnel lengths to become independent of this choice. The bubble is placed near the end of the tunnel based on the observations in the microscopy images (Caskey *et al.* 2009*a*). The initial distance of the bubble centre from the tunnel δx_{b0} is varied to study the effect of initial configuration on tunnelling rate. However, $\delta x_{b0} = D_i/2$, unless otherwise noted, and nearly all of the results concern a behaviour that has become independent of the placement. The density ρ outside the bubble is uniformly $1000\,\mathrm{kg\,m^{-3}}$ as appropriate for tissues or hydrogels (Maxwell *et al.* 2010). The viscosity of the degraded material is taken to be water-like, with $\mu_1 = 0.001\,\mathrm{Pa\,s}$. The viscosity and damage threshold of the material are motivated by the characteristics of common tissue-mimicking gels. The viscosity of the undegraded material is varied from $\mu_2 = 0.002\,\mathrm{Pa\,s}$
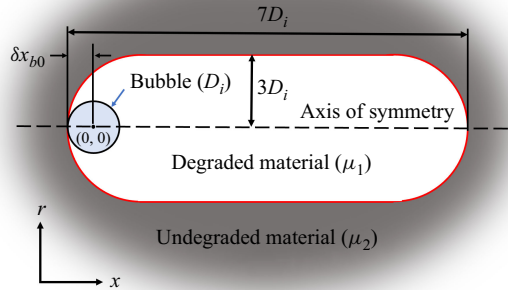
Figure 2. Proto-tunnel initial condition.

to 0.025 Pa s (Hamaguchi & Ando 2015; Murakami *et al.* 2021), which corresponds to the ratio $\mu^* = \mu_2/\mu_1 = 2\text{--}25$.

The tensile stretch limit (see § 2.3) is $\lambda_f = 1.5$, which is similar to tissue-mimicking hydrogels (Gent & Wang 1991; Barrangou, Daubert & Foegeding 2006). The surface tension on the bubble surface is $\sigma = 0.073 \, \text{N m}^{-2}$. The frequency of the driving acoustic excitation ranges from $f = 1$ to $4 \, \text{MHz}$, which is within the range of therapeutic HIFU (Vlaisavljevich *et al.* 2015). Corresponding ultrasound wavelengths 0.185–1.48 mm are large with respect to the bubble diameter and so are represented as a uniform far-field pressure that cycles as (Plesset & Prosperetti 1977; Gaudron, Warnez & Johnsen 2015)

$$p_\infty = p_0 - p_a \sin(2\pi f t), \tag{2.1}$$

where $p_0 = 10^5 \, \text{Pa}$ is the ambient mean pressure. This treatment of the acoustic pressure is consistent with common practice (Prosperetti & Lezzi 1986; Calvisi *et al.* 2007; Wang & Blake 2011), including bubble dynamics driven by travelling acoustic waves (Calvisi *et al.* 2007). Because p_∞ is uniform, the bubble does not experience an acoustic radiation force (King 1934). The initial bubble pressure is $p_{b0} = 20p_0$, which corresponds to an equilibrium bubble diameter (D_0) of 1.6 µm. An elevated initial pressure was selected to show that the model can represent bubble-collapse jetting and its accelerated damage, which $p_{b0} = 20p_0$ produces, but results will show that this jetting gives way to a non-jetting steady tunnelling. Long-time tunnelling rates are confirmed to be independent of this initial pressure, and tunnelling does not occur without subsequent acoustic excitation. The amplitude of the acoustic excitation p_a varies from 0.15 to 0.35 MPa, which loosely emulates the expected conditions where tunnelling is seen in tissue outside the focus region in HIFU therapeutic procedures (Maxwell *et al.* 2010). The equilibrium bubble diameter D_0 and the ambient pressure p_0 yield an inviscid linear spherical resonance frequency

$$f_n = \frac{1}{\pi D_0} \sqrt{\frac{3 p_0 \gamma}{\rho}} \approx 4 \, \text{MHz}. \tag{2.2}$$

A reference velocity scale is associated with the velocity of the bubble interface during Rayleigh collapse (Rayleigh 1917; Curtiss *et al.* 2013; Han *et al.* 2015; Ohl *et al.* 2015):

$$u_0 \equiv \sqrt{\frac{\Delta p}{\rho}} \approx 10 \, \text{m s}^{-1}, \tag{2.3}$$

where $\Delta p \sim 10^5$ Pa represents the difference in the pressure within the expanded bubble ($p_b \approx 0.2 \times 10^5$ Pa) and mean ambient pressure ($p_0 \approx 10^5$ Pa). The reference parameters D_0, p_0, u_0 and f_n are used for subsequent non-dimensionalisation. The Weber number is

$$We_D = \frac{\rho u_0^2 D_0}{\sigma}, \tag{2.4}$$

and a Reynolds number to characterise the flow in the high-viscosity undegraded material is

$$Re_D = \frac{\rho \dot{R}_m D_m}{\mu_2}, \tag{2.5}$$

where D_m is the diameter of the bubble when the rate of change of its radius $\dot{R} = \dot{R}_m$ is maximum. For a deformed bubble, D_m and $\dot{R}_m$ are based on a sphere of equal volume.

The elastic versus viscous stresses can be estimated for a Kelvin–Voigt material. Shear modulus $G = 1$ kPa and shear viscosity $\mu = 0.01$ Pa s is considered (Murakami *et al.* 2021). The nominal diameter of the bubble is taken as $D = 1\,\mu\text{m}$. The bubble is excited by a sinusoidal far-field acoustic excitation at $f = 1$ MHz and amplitude $p_a = 10^5$ Pa. A scale for strain (ε) and strain rate ($\dot{\varepsilon}$) in the material surrounding the oscillating bubble is given by

$$\varepsilon \equiv \frac{u_0}{Df} \approx 10 \tag{2.6}$$

and

$$\dot{\varepsilon} \equiv \frac{u_0}{D} \approx 10^7 \text{ s}^{-1}, \tag{2.7}$$

respectively. Therefore, an elastic stress scale is

$$\tau_e \equiv G\varepsilon \equiv \frac{Gu_0}{Df} \approx 10^4 \text{ Pa}, \tag{2.8}$$

and the corresponding viscous stress scale is

$$\tau_v \equiv \mu\dot{\varepsilon} \equiv \frac{\mu u_0}{D} \approx 10^5 \text{ Pa}. \tag{2.9}$$

Therefore, the Wissenberg number of the flow is $Wi = \tau_e/\tau_v = 0.1$, so viscous effects are anticipated to dominate elastic effects. A more sophisticated model might better characterise the potentially multiple continuum and molecular time scales of the material degradation and elastic resistance, but this loose estimate is sufficient for justifying a viscous-only model for the present purposes. An approximate factor of ten is significant, on top of which it should be recognised that large strains do not yield large elastic stresses because of the material degradation. A more specific analysis of a Rayleigh–Plesset equation modified for a degrading Kelvin–Voigt material suggests that viscous effects will exceed elastic effects by a factor of 500 with these same viscous, elastic and degradation parameters. It was shown in a previous study (Murakami *et al.* 2021) that the amplitude of oscillation of small bubbles with an equilibrium radius of approximately $10\,\mu\text{m}$ is similar in a Kelvin–Voigt viscoelastic material and Newtonian viscous fluid with the same viscosity.

2.3. *Governing equations*

The incompressible fluid outside the bubble flows according to

$$\rho \left[\frac{\partial \boldsymbol{u}}{\partial t} + \boldsymbol{u} \cdot \boldsymbol{\nabla} \boldsymbol{u} \right] = -\boldsymbol{\nabla} p + \boldsymbol{\nabla} \cdot \boldsymbol{\tau}, \tag{2.10}$$

$$\boldsymbol{\nabla} \cdot \boldsymbol{u} = 0, \tag{2.11}$$

where ρ is the density, $\boldsymbol{u}$ is the velocity, p is the pressure and $\boldsymbol{\tau}$ is the deviatoric stress tensor. The fluid is a mixture of the degraded and the undegraded Newtonian components, so

$$\boldsymbol{\tau} = \bar{\mu} \left(\boldsymbol{\nabla} \boldsymbol{u} + \boldsymbol{\nabla} \boldsymbol{u}^T \right) \tag{2.12}$$

with mixture viscosity

$$\bar{\mu} = \frac{(1 - \phi)}{2} \mu_1 + \frac{(1 + \phi)}{2} \mu_2, \tag{2.13}$$

where $\phi = -1$ indicates fully degraded material and $\phi = 1$ undegraded material. Material is tracked by an advection equation:

$$\frac{\partial \phi}{\partial t} + \boldsymbol{\nabla} \cdot (\boldsymbol{u} \phi) = b \left[\nabla^2 \phi + \frac{\phi \left(1 - \phi^2 \right)}{W^2} - |\boldsymbol{\nabla} \phi| \boldsymbol{\nabla} \cdot \left(\frac{\boldsymbol{\nabla} \phi}{|\boldsymbol{\nabla} \phi|} \right) \right] - R_d I_d (1 + \phi). \tag{2.14}$$

Experiments show a sharp boundary between the degraded and the undegraded material (Caskey *et al.* 2009*a*; Maxwell *et al.* 2010; Lundt *et al.* 2017), which is maintained in the simulations. The first term on the right-hand side is a common model to ensure that a sharp hyperbolic-tangent-like ϕ profile is preserved along the normal to the boundary (Folch *et al.* 1999; Sun & Beckermann 2007). Earlier, this method was found to preserve the sharpness of the interface with excellent mass conservation (Sun & Beckermann 2007). We shall see in § 4.2 that any mass error, which in this case would cause artificial degradation (or repair) of the material, is insufficient to show any sign of tunnelling. The model parameters W and b mediate the target thickness of this interface and the strength of the sharpening. Except when noted, W is twice of the minimum mesh spacing Δx, and the sharpening parameter is (Sun & Beckermann 2007)

$$b = \alpha_b \frac{\Delta x^2}{\Delta t}, \tag{2.15}$$

where $\alpha_b = 6.0 \times 10^{-5}$. The bubble dynamics and tunnelling are insensitive to W and α_b in the range of $\pm 50\,\%$ of these standard values.

The second term on the right-hand side of (2.14) models degradation. This degradation model is a low-elasticity limit of the established model of Shanthraj *et al.* (2016). The rate coefficient is $R_d = 20 f_n$, where f_n is the natural frequency of the bubble, and the indicator,

$$I_d = \begin{cases} 0 & \text{if } \lambda_m < \lambda_f \\ 1 & \text{if } \lambda_m \geqslant \lambda_f \end{cases}, \tag{2.16}$$

is activated where the maximum of the principal stretches $\lambda_m = max(\lambda_1, \lambda_2, \lambda_3)$ exceeds the stretch threshold λ_f. As this linear maximum-stretch model obviously neglects many factors that would mediate degradation of a real material (Movahed *et al.* 2016; Milner & Hutchens 2021), it might be quantitatively incorrect for complex materials. Nevertheless,

it is expected to afford the correct phenomenology, as will be seen. Closer quantitative comparisons with rates might require refinements to the material damage model.

The principal stretches depend on the deformation from the $Z = (X, R, \Theta)$ initial material coordinates to the $z = (x, r, \theta)$ current coordinate as mapped by the deformation gradient tensor:

$$F = \frac{\partial z}{\partial Z}. \tag{2.17}$$

The material derivative of F is

$$\dot{F} = \frac{\partial F}{\partial t} + u \cdot \nabla F = \nabla u \cdot F, \tag{2.18}$$

which evolved in time along with (2.10), (2.11) and (2.14) to track deformation (Liu & Walkington 2001; Kamrin, Rycroft & Nave 2012). The principal stretches $(\lambda_1, \lambda_2, \lambda_3)$ are the square-root of eigenvalues of the right Cauchy–Green tensor: $C = F^T \cdot F$. The maximum principal strain, which will be analysed, is

$$\varepsilon_{max} = \max \left(\frac{\lambda_1^2 - 1}{2}, \frac{\lambda_2^2 - 1}{2}, \frac{\lambda_3^2 - 1}{2} \right). \tag{2.19}$$

Therefore, the material degradation model described in (2.14) through (2.16) limits ε_{max} to a maximum of $(\lambda_f^2 - 1)/2$ in the undegraded material.

2.4. *Bubble representation*

For an homogeneous inviscid adiabatic gas, the pressure p_b and volume V_b of the bubble follows

$$p_b V_b^\gamma = p_{b0} V_{b0}^\gamma, \tag{2.20}$$

where V_{b0} is the initial volume of the bubble and we take $\gamma = 1.4$. The bubble pressure contributes to the boundary condition for the liquid on the bubble surface.

The bubble interface is treated differently than the material ϕ boundary. It is represented by the $\psi = 0$ level set of advected field variable ψ,

$$\frac{\partial \psi}{\partial t} + u \cdot \nabla \psi = 0, \tag{2.21}$$

with a constrained fourth-order least-squares method, consistent with the discretisation, that enforces kinematic and dynamic conditions. The continuity of the velocity,

$$[u] = 0, \tag{2.22}$$

and the deformation gradient tensor,

$$[F] = 0, \tag{2.23}$$

are the kinematic conditions at the bubble interface, with the liquid–gas $(l\text{–}g)$ jump condition for any variable χ defined as

$$[\chi] = \chi_l - \chi_g. \tag{2.24}$$

The two dynamic interface conditions needed for axisymmetric flow without swirl are

$$p_l = p_g + 2\mu_l \frac{\partial u_n}{\partial n} + \sigma (\kappa_1 + \kappa_2) \tag{2.25}$$

and

$$\mu_l \left(\frac{\partial u_s}{\partial n} + \frac{\partial u_n}{\partial s} \right) = 0, \tag{2.26}$$

where n is the local normal coordinate and s is the relevant local tangent coordinate. The two principle curvatures of the bubble interface, κ_1 and κ_2, are

$$\kappa_1 = \nabla \cdot \left(\frac{\nabla \psi}{|\nabla \psi|} \right) \qquad \text{and} \qquad \kappa_2 = \frac{1}{r} \frac{\psi_r}{|\nabla \psi|}. \tag{2.27}$$

Bubble contact with the undegraded material is minimal, so the choice of

$$\frac{\partial \phi}{\partial n} = 0 \tag{2.28}$$

on the bubble surface is inconsequential.

2.5. *Discretisation*

The flow equations (2.11) and (2.10) are discretised on a staggered mesh using a standard second-order fractional-step method (Chorin 1967) with second-order Runge–Kutta time integration of (2.10), (2.14), (2.18) and (2.21). The time step size is computed adaptively such that the following stability criteria is satisfied (Kang, Fedkiw & Liu 2000):

$$\Delta t \frac{C_c + C_v + \sqrt{(C_c + C_v)^2 + 4C_{sft}^2}}{2} \leqslant 0.5, \tag{2.29}$$

where

$$C_c = \frac{u_{max} + v_{max}}{\Delta x}, \quad C_v = \left(\frac{\overline{\mu}}{\rho} \right) \left(\frac{4.0}{\Delta x^2} \right), \quad C_{sft} = \sqrt{\frac{\sigma |\kappa_1 + \kappa_2|}{\Delta x^2}}, \tag{2.30}$$

and u_{max} and v_{max} are the maximum magnitudes of the velocity components in the computation domain. The advection terms in (2.14), (2.18) and (2.21) are discretised using a fifth-order WENO scheme (Jiang & Shu 1996). The use of the fifth-order WENO method for discretisation of the advection term $u \cdot \nabla F$ in (2.18) sufficiently preserved the incompressibility constraint ($\nabla \cdot F = 0$). We also note that the degradation makes the accuracy of F immaterial before widespread and strong gradients can arise.

The interfacial conditions at the bubble surface (2.22)–(2.28) are enforced by extending the u, p, F and ϕ fields from the liquid phase near the interface to the grid points in the gas phase across the interface (Caiden, Fedkiw & Anderson 2001; Popinet & Zaleski 2002) using a fourth-order least-square reconstruction that is constrained to be divergence-free on the boundary, with (2.25) and (2.26) imposed as linear constraints in the least-squares fit. The pressure in the liquid and the gas are coupled at the bubble interface through (2.25). The F and ϕ fields are extrapolated with appropriate constraints into the bubble with a second-order least-squares reconstruction, though these are not particularly important on the bubble. This scheme is implemented in the AMReX adaptive mesh refinement engine (Zhang *et al.* 2019).

The discretised domain spans $\pm 240 D_0$ in x and extends radially to $r = 240 D_0$, which provides results that are independent of the domain size. The symmetry axis is $r = 0$. The pressure on the other three boundaries is p_∞ from (2.1) with $\nabla u \cdot n = 0$ (where n is unit vector normal to the boundary) to allow fluid flow through the domain boundary. Adaptive mesh refinement provides resolution near the bubble ($\psi = 0$) and the damage boundary ($\phi = 0$). The coarsest mesh has $D_0 = 0.13 \Delta x$ with resolution doubled at every level of refinement.
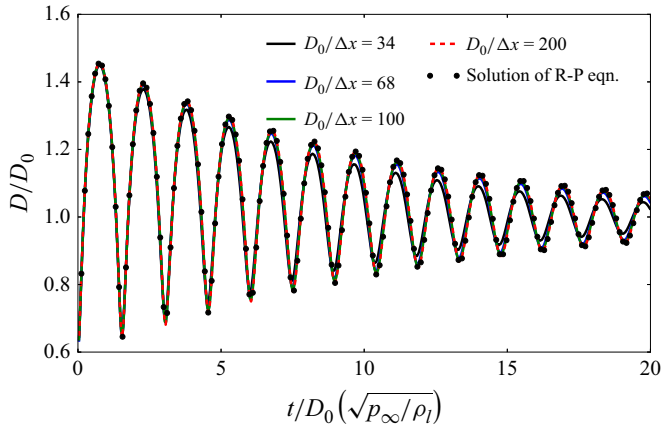
Figure 3. Comparison of the axisymmetric adaptive-mesh solver with an accurate (spherical) free-space Rayleigh–Plesset (2.31) solution for the evolution of the bubble diameter $D(t)$. The initial condition is $R(0) = 5.0\,\mu\text{m}$ with $\mu = 0.002\,\text{Pa s}$ and $p_{b0} = 10 p_0$.

2.6. *Demonstration: spherical bubble oscillations*

The accuracy of the method, domain size and discretisation, particularly bubble-volume conservation, is assessed for the same computational domain against an accurate numerical solution of the infinite-domain Rayleigh–Plesset equation,

$$R\ddot{R} + \frac{3}{2}\dot{R}^2 = \frac{1}{\rho}\left[p_{b0}\left(\frac{R_0}{R}\right)^{3\gamma} - p_\infty - \frac{4\mu\dot{R}}{R} - \frac{2\sigma}{R}\right], \quad (2.31)$$

where $R(t)$ is the bubble radius. The initial bubble radius $R(0) = 5\,\mu\text{m}$ and its initial pressure is $p_{b0} = 10 p_\infty$ with $\mu = 0.002$ Pa s and $\sigma = 0.072\,\text{N m}^{-1}$. The equilibrium bubble diameter D_0 in this case is $16.7\,\mu\text{m}$. The diameter $D(t)$ shows only a slow accumulation of error over many cycles in figure 3. The decay of amplitude due to viscous dissipation is also well reproduced. Errors do, of course, accumulate with time, though even the coarsest resolution might be considered to provide sufficient accuracy for our objectives.

The L_2 error in calculation of the bubble diameter over the duration of the calculation is

$$\epsilon_{L_2} = \frac{\int_0^{30 D_0 \sqrt{\frac{\rho_l}{p_\infty}}} \left(D\left(t\right) - D_{rp}\left(t\right)\right)^2\,\text{d}t}{\int_0^{30 D_0 \sqrt{\frac{\rho_l}{p_\infty}}} D_{rp}\left(t\right)^2\,\text{d}t}. \quad (2.32)$$

This L_2 error decreases from 0.0271 to 0.0022 for resolution increase from $D_0/\Delta x = 34$ to 200, with a well-fitted $\epsilon_{L_2} \propto \Delta x^{1.4}$ behaviour. Even though most components of the algorithm are at least second order, full second-order convergence for this quantity is not expected because it entails so many coupled components. However, convergence is sufficient for our goals, as is the 1.2 % error for $D_0/\Delta x = 68$, which is the main resolution we use. This case also was used to confirm that a computation domain extending to $r = 60 D_0$ from the bubble centre was sufficient to show domain size independence over 14 bubble cycles. With the adaptive meshing, extending to $r = 240 D_0$ provided additional confidence of this at a modest cost. To confirm implementation and selected resolution, the evolution of a pressurised bubble near a wall was also simulated with these same
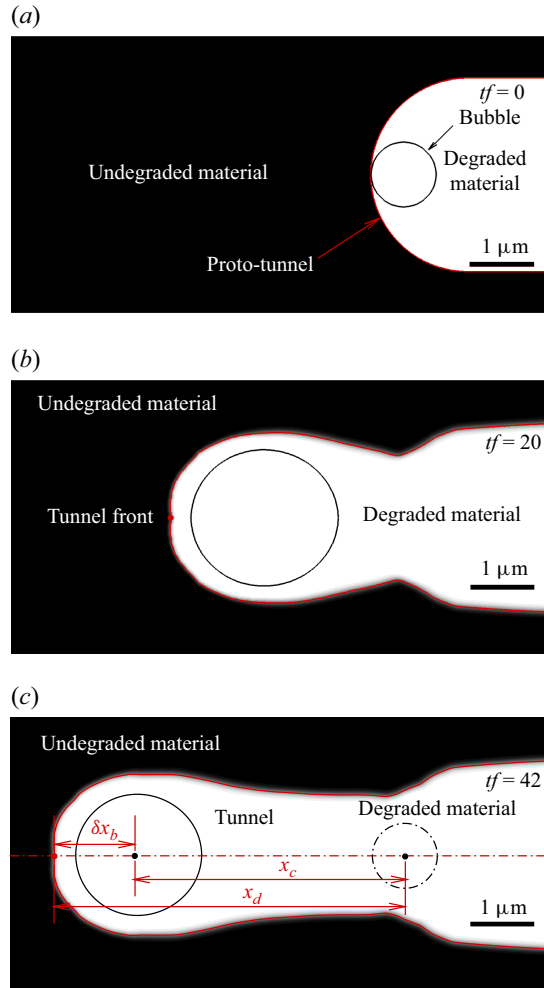
(*a*)

(*b*)

(*c*)

Figure 4. Establishment of a tunnel through the undegraded high viscosity fluid (black) for $p_a = 2.5p_0$, $p_{b0} = 20p_0$, $f = f_n$, $\mu^* = \mu_2/\mu_1 = 10$ and $\lambda_f = 1.5$ at (*a*) $tf = 0$, (*b*) $tf = 20$ and (*c*) $tf = 42$. The bubble interface $\psi = 0$ is the black contour, which is dash-dotted to indicate its initial position in panel (*c*).

parameters and confirmed to match closely the Popinet & Zaleski (2002) simulations that also reproduce the Lauterborn & Ohl (1997) experiment.

3. Bubble tunnelling

Taking $p_a = 2.5p_0$, $f = f_n$ and $\mu^* = 10$ yields tunnelling, the mechanisms of which are analysed in this section. Parametric dependencies are considered in the following sections. Figure 4 visualises early development as the bubble travels approximately $2.5D_0$ over 42 cycles, extending the initial proto-tunnel. The centre-of-mass location of the bubble x_c, degradation front location x_d and the distance of the centre of mass of the bubble from the degradation front $\delta x_b = x_c - x_d$ are defined in figure 4(*c*). The evolution of x_c, x_d and bubble volume V_b are shown in figure 5. The bubble volume V_b tracks a nearly periodic expand-and-collapse cycle after approximately four cycles, and there is steady tunnelling after approximately 10 cycles. The rate of growth of the tunnel to the left $u_D = 0.034u_0$
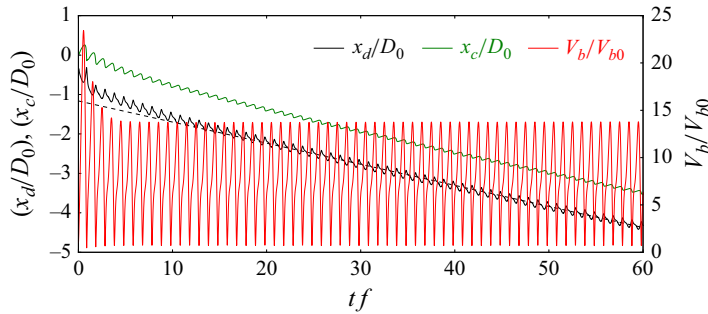
Figure 5. Evolution of the degradation front x_d (defined in figure 4c), the centre of mass of the bubble x_c and the volume of the bubble V_b during tunnelling are shown. The acoustic excitation and the material parameters in this calculation are $p_a = 2.5p_0$, $p_{b0} = 20p_0$, $f = f_n$, $\mu^* = 10$ and $\lambda_f = 1.5$.

is computed from the slope of a least-squares linear fit to $x_d(t)$ between $tf = 40$ and 100 (figure 5). Figure 6(a) confirms that u_D converges with increasing mesh resolution and that the $D_0 = 68\Delta x$ case is close to (7.9 % less) the highest mesh density ($D_0 = 136\Delta x$) case. Similarly, $V_b(t)$ in figure 6(b) shows mesh independence for $D_0 \gtrsim 68\Delta x$. The results obtained using the mesh resolution corresponding to $D_0 = 68\Delta x$ are used for the analysis of the tunnelling phenomenon.

The initial and the steady tunnelling differ qualitatively. Tunnel growth during the first cycle ($tf = 0.03 - 1.05$) and for steady tunnelling ($tf = 38.5 - 39.5$) are shown in figures 7 and 8.

3.1. *Initial tunnelling: material degradation due to jetting collapse of the the bubble*

The initial high pressure in the bubble leads to its expansion followed by a jetting collapse. Figure 7(a) shows the initial expansion of the bubble with minimum $p_b = 0.24p_0$ before reversing at $tf \approx 0.5$. Figure 7(b) shows the corresponding strain in the surrounding material. The subsequent collapse is asymmetric. Figure 7(c) shows that the velocity of the bubble surface is smaller adjacent to the undegraded viscous material, which leads to the formation of a jet towards the undegraded material (figure 7d). This jet eventually crosses the bubble, transiently forming a toroidal bubble (figure 7e). Figures 7(e) and 7(f) show that the undegraded material adjacent to the bubble is strained as the jet impinges on it. As the toroidal bubble expands, the liquid bridge at the centre of the bubble breaks, as seen in figure 7(g). Finally, figure 7(h) shows the rebound to a nearly spherical expanded shape. During this expansion, the undegraded material around the bubble is also stretched, causing further degradation. Although jetting is important in this initial phase for this initial condition, it does not persist into the steady tunnelling phase.

3.2. *Steady tunnelling: the move-expand-stretch(-repeat) mechanism*

The bubble dynamics during the steady growth of the tunnel are visualised in figure 8. Figure 8(a) shows the peak bubble volume when velocity is small and high strain extends ahead of the bubble, degrading the material. The low bubble pressure initiates the subsequent collapse (figure 8b), during which the acceleration of the bubble interface towards the bubble centre is non-uniformly impeded by the viscosity of the material, and the surface furthest from the undegraded material achieves the highest speed inward. The resulting asymmetry of the bubble shape is measured by its
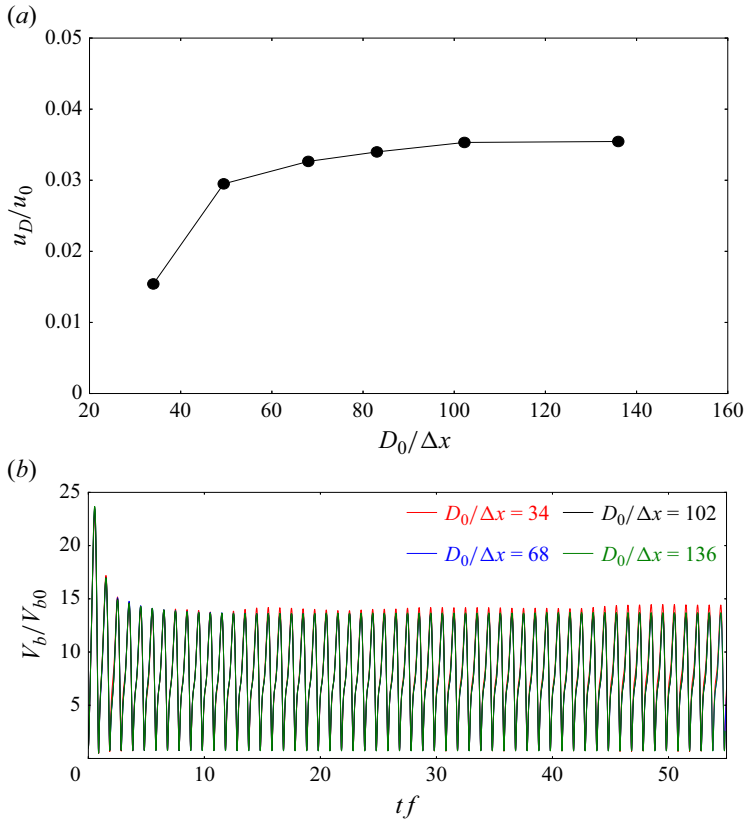
Figure 6. (*a*) Rate of tunnel growth u_D and (*b*) bubble volume V_b for increasing grid resolution for $p_a = 2.5p_0$, $f = f_n$ and $\mu^* = 10$.

sphericity

$$\Psi\,(t) = \frac{\pi^{\frac{1}{3}}[6V_b(t)]^{\frac{2}{3}}}{A_b\,(t)}, \tag{3.1}$$

where A_b is its surface area. It is nearly spherical ($\Psi \approx 1$) at $tf = 38.5$ near maximum volume (figure 8*a*). However, as the bubble starts to collapse, Ψ decreases, but the minimum is only $\Psi_{min} \approx 0.95$ at $tf = 38.8$. The corresponding shape of the bubble is shown in figure 8(*c*). Formation of a high speed re-entrant jet during steady tunnelling is not observed in this calculation. Figure 8(*c*) shows thats the bubble is further from the leading edge of the tunnel, which reduces the asymmetry in the viscous resistance it experiences. The cycle-averaged distance of the bubble centre from the tunnel end increases to $\overline{\delta x_b} = \overline{x_c - x_d} \approx 0.84D_0$. At this distance, the asymmetry in the viscous resistance continues to cause the bubble to deform, though insufficiently for jetting collapse. The velocity vectors in figure 8(*c*), at the minimum bubble volume, indicate a net flow of the degraded material towards the leading end of the tunnel. Its momentum to the left is quantified by

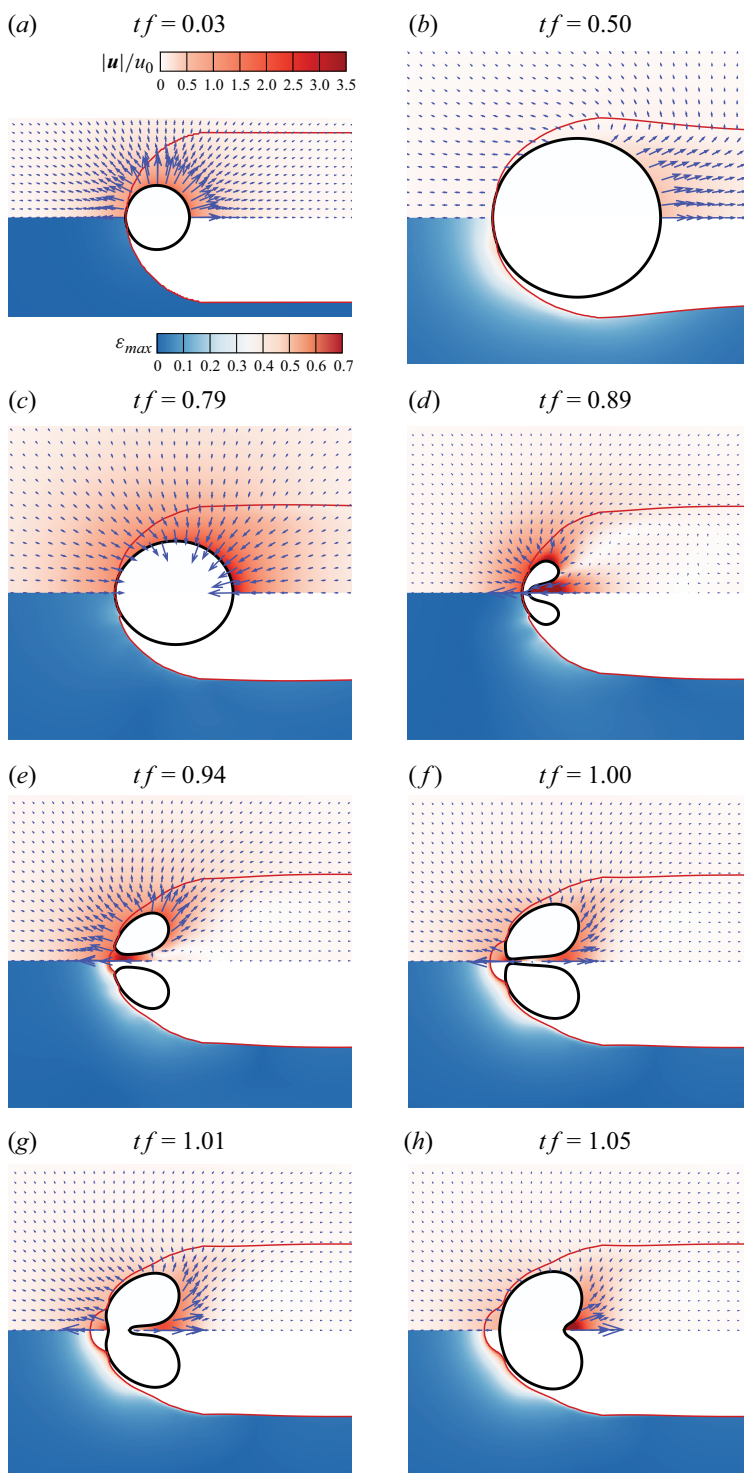$$M_{-x} = -\int_{V_c} \frac{1-\phi}{2}\rho u\,\mathrm{d}V, \tag{3.2}$$

Figure 7. Bubble dynamics for $p_a = 2.5 p_0$, $f = f_n$ and $\mu^* = 10$ during the first excitation cycle for the times as labelled. The boundary of the undamaged material is red and the boundary of the bubble is black. The velocity field at the top of each frame is shown with vectors and increasing dark levels for larger $|\boldsymbol{u}|$. The bottom of each frame shows the local maximum principal strain field ε_{max}.
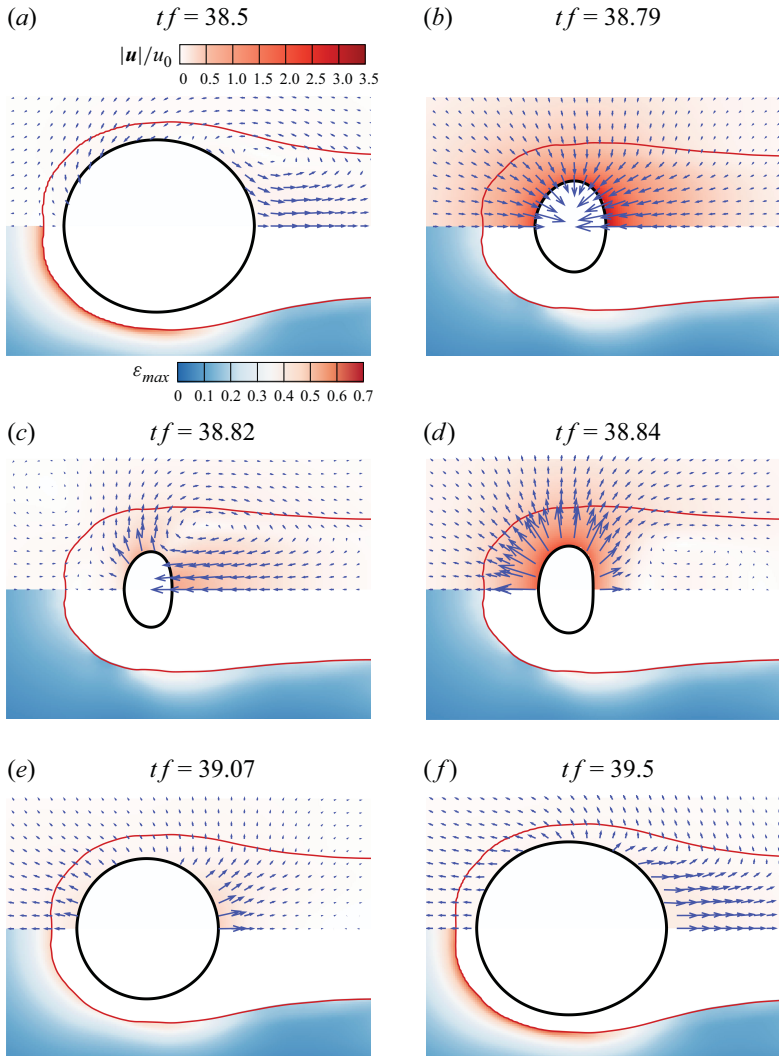
Figure 8. Evolution of the bubble and the tunnel over an excitation cycle for $p_a = 2.5 p_0$, $f = f_n$ and $\mu^* = 10$ during steady tunnelling, approximately 35 cycles after the times visualised in figure 7. The upper portions show velocity vectors and $|\boldsymbol{u}|$, and the lower portions show peak principle strain ε_{max}.

where V_c is the computational domain. Figure 9(a) shows that M_{-x} peaks during the collapse, pulling the bubble along the tunnel and keeping it near the growing tunnel front. The small net displacement of the bubble during its collapse is shown in figure 9(b). The time series plot of x_c in figure 9(c) also shows the asymmetric fast movement of the bubble centre during the collapse.

The subsequent rebound of the bubble from its collapsed state strains the undegraded material surrounding the tunnel end. The ε_{max} visualised in figure 8 shows increase in ε_{max} at the tunnel end as the bubble expands. It is only during the expansion phase, seen in figures 8(a), 8(e) and 8(f), that the undegraded material around the bubble is strained beyond its threshold λ_f. The growth of the tunnel over one oscillation is also visualised in figure 9(b). The history of x_d and x_c in figure 9(c) shows that the bubble travels left during the collapse phase of the bubble. In sum, it is a move-expand-stretch(-repeat) mechanism that grows the tunnel.
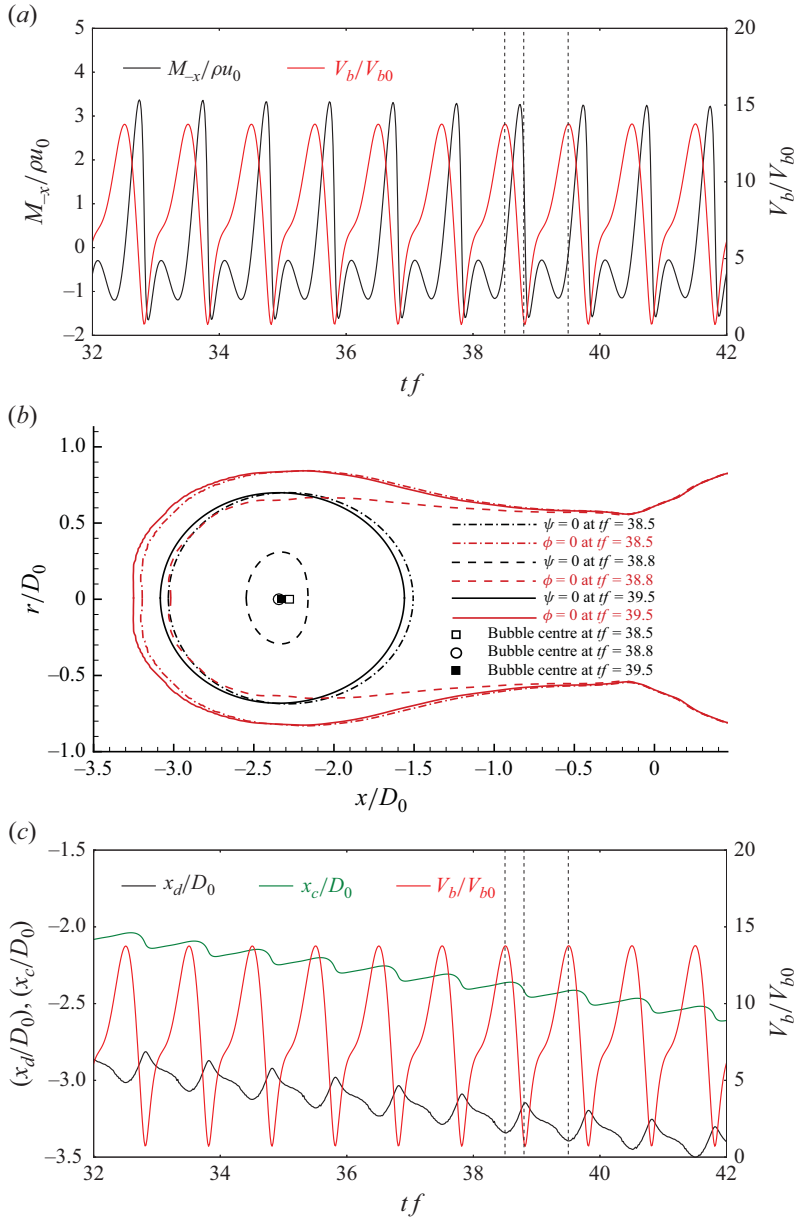
Figure 9. Steady tunnelling behaviour: (*a*) the time evolution of normalised net momentum M_{-x} from (3.2) of the degraded material along and the bubble volume V_b; (*b*) the displacement of the bubble interface (black line) and the interface between the undegraded and the degraded material (red line) during one complete cycle of oscillation between $tf = 38.5$ and 39.5 of the bubble; and (*c*) the time evolution of x_c, x_d and V_b.

4. Dependence on material properties

Changing the undegraded material viscosity μ_2, damage threshold λ_f, bubble surface-tension σ and the acoustic forcing changes the tunnelling rate with some interesting threshold behaviours. However, the basic mechanisms of tunnelling do not change qualitatively.
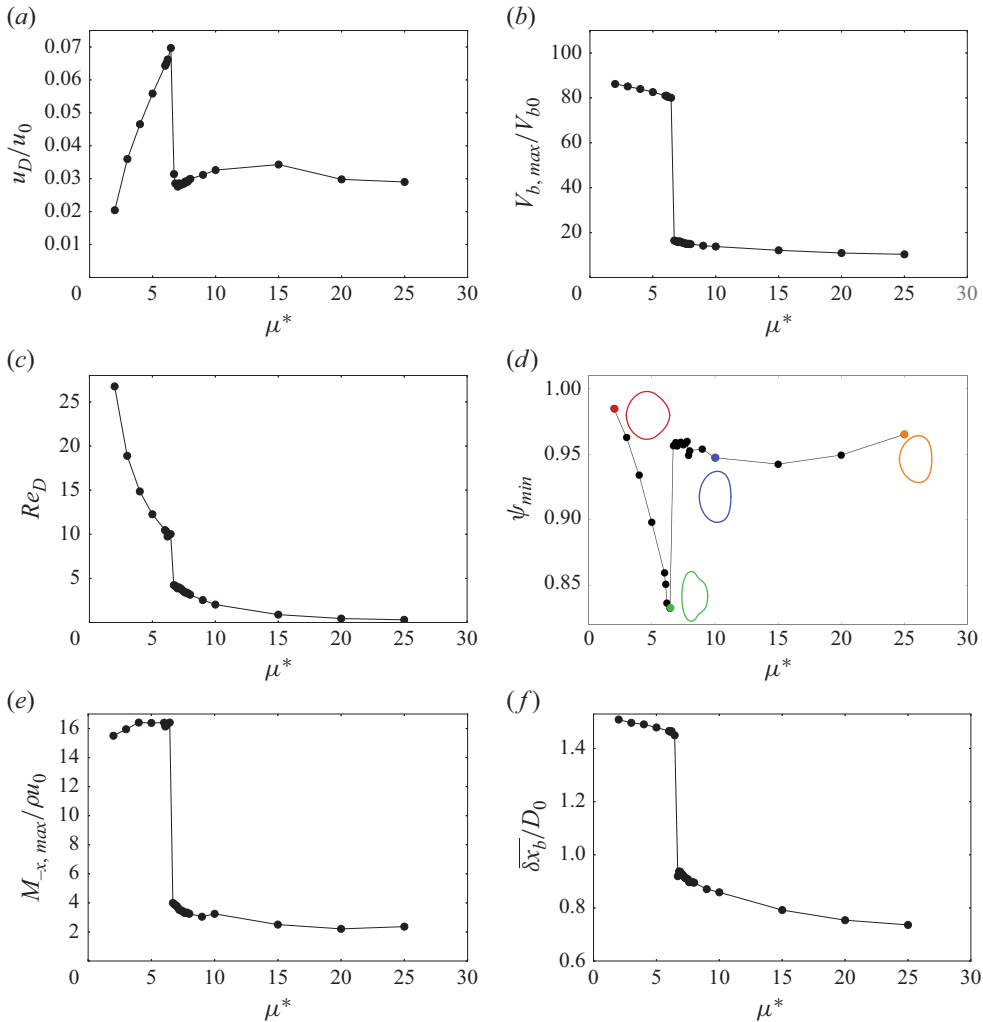
Figure 10. Effect of μ^* on tunnelling: (*a*) tunnelling speed u_D; (*b*) maximum bubble volume $V_{b,max}$; (*c*) Re_D; (*d*) minimum sphericity Ψ during the stable oscillation; (*e*) peak momentum $M_{-x,max}$ of the degraded material towards the tunnel end during bubble collapse; and (*f*) average distance $\overline{\delta x_b}$ of the bubble centre from the tunnel end.

4.1. *Effect of material viscosity μ^**

Varying $\mu^* = \mu_2/\mu_1$ from 2 to 25, keeping $\mu_1 = 0.001$ Pa s, shows a jump in the tunnelling rate (figure 10*a*): u_D increases approximately linearly from $\mu^* = 2$ to 6.45, which is unexpected since greater viscosity might be anticipated to resist strain. It then surprisingly drops by half at an apparent μ^* threshold between 6.45 and 6.7. For larger μ^*, it changes only modestly, suggesting an apparently constant value for $\mu^* \gtrsim 20$. The details of the move-expand-stretch mechanism explain this behaviour. The tunnel growth rate is determined by two factors: (1) the bubble translation rate towards the growing tunnel end during its collapse phase and (2) the extent of strain-induced degradation during its subsequent expansion. Increasing the viscosity of the undegraded material influences both of these, which in turn leads to the non-monotonic tunnelling speed. The drop in tunnelling rate corresponds to a significant drop in maximum bubble volume $V_{b,max}$ due to
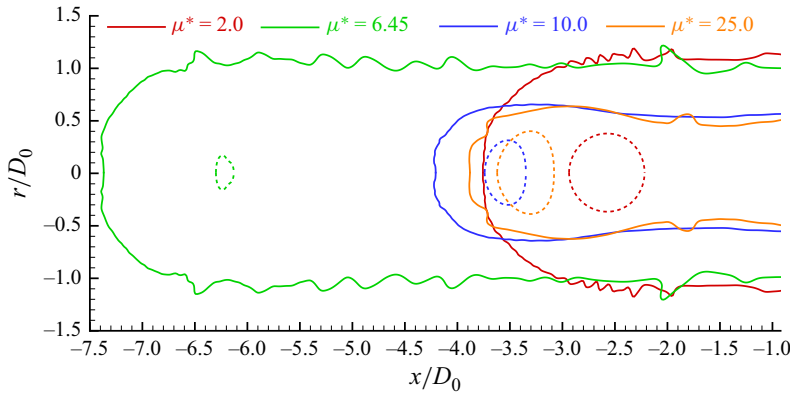
Figure 11. Shapes of the tunnels and the bubble at $tf = 42.8$ for $\mu^* = 2$, 6.45, 10 and 25 are shown with $\phi = 0$ (solid) and $\psi = 0$ (dashed) contours.
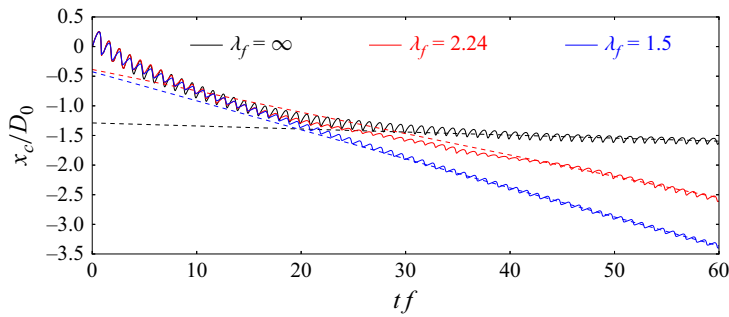

Figure 12. Tunnelling for different stretch degradation threshold λ_f. The dashed lines are linear fits.

a switch from inertia to viscosity-dominated dynamics. Figure 10(*b*) shows that the $V_{b,max}$ abruptly decreases by a factor of 5, as seen from spherical models, for which the viscous resistance suddenly overwhelms inertial expansion (Freund 2008; Movahed *et al.* 2016). This is reflected in $Re_D \approx 1$ for $\mu^* \gtrsim 6.5$ in figure 10(*c*). Increasing μ^* also increases environment asymmetry, inducing asphericity in bubble shape during its inertial collapse (figure 10*d*). This has a corresponding increase in the net flow of the degraded material towards the growing end of the tunnel, reflected in the maximum value of M_{-x} ($M_{-x,max}$) in figure 10(*e*), increasing the translation of the bubble during the collapse phase.

The maximum expansion of the bubble is suppressed for $\mu^* \gtrsim 6.5$, so the tunnel extension due to the expansion of the bubble and the bubble movement in the subsequent collapse phase are both suppressed due to the high viscosity of the undegraded material. However, even with the suppressed expansion, it still stretches the undegraded material beyond λ_f because the bubble in this case sits closer to the tunnel end. Specifically, figure 10(*f*) shows that $\overline{\delta x_b}$ also has a step decrease near $\mu^* = 6.5$. The visualisations in figure 11 show the lengths and shapes of the tunnel at $tf \approx 42.8$ for selected μ^*. The tunnels are wider for $\mu^* \lesssim 6.5$ due to the greater expansion.

4.2. *Effect of stretch threshold λ_f*

Stretch thresholds $\lambda_f = 1.50$, 2.24 and ∞ (no degradation) in figure 12 show, as expected, that bubble moves less for higher λ_f. The expansion is more suppressed due to the viscous

λ_f	u_D/u_0	$V_{b,max}/V_{b0}$	$\overline{\delta x_b}/D_0$
∞	0.0009	9.81	0.30
2.24	0.0242	12.58	0.76
1.50	0.0322	13.80	0.81

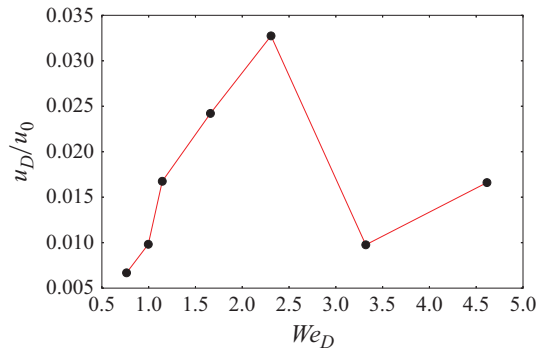Table 1. Dependence on damage threshold λ_f.

Figure 13. Effect of the bubble surface tension on the tunnelling rate for $p_a = 2.5p_0$, $p_{b0} = 20p_0$, $f = f_n$, $\mu^* = 10$ and $\lambda_f = 1.5$.

resistance when λ_f is increased, with the maximum volume of the bubble decreasing for larger λ_f (see table 1). However, the mean distance of the bubble centre from the tunnel end $\overline{\delta x_b}$ decreases at higher λ_f, so the tunnel still grows with bubble expansion in each cycle. The long time to reach the equilibrium growth rate in figure 12 for $\lambda_f = 2.4$ is due to the relatively long time it takes for the bubble to reach its equilibrium $\overline{\delta x_b}$. The $\lambda_f \rightarrow \infty$ case is not realistic, but it is informative about the overall model. In this case, there is no degradation, but the bubble translates slowly into the high viscosity region. It stops when its environment is effectively symmetric once it travels a few diameters from the proto-tunnel initial condition.

4.3. *Effect of surface-tension σ*

The water–gel system that motivated our parameter selection would give $We_D = 2.31$. Figure 13 shows that higher surface tension (smaller We_D) suppresses tunnelling. This is because it suppresses expansion of the bubble and also its migration along the tunnel because the bubble remains more spherical. The behaviour for larger We_D shows the same sudden change of behaviour associated with discontinuous dependence on μ^*, but likely involves additional factors. The bubble becomes unstable for very low surface tensions, which makes the axisymmetric model less relevant, so this is not explored in detail.

5. Dependence on the acoustic excitation parameters

Larger p_a increases bubble expansion and thereby tunnelling rate u_d (figure 14a), and leads to the formation of wider tunnels because more material is strained by the larger bubbles (figure 14c), which loosely matches observations of wider tunnels for strong excitation (Caskey *et al.* 2009b). Figure 14(a) shows a sudden increase in u_d and $V_{b,max}$ when p_a exceeds approximately $2.75p_0$. This marks the transition from viscous to inertial
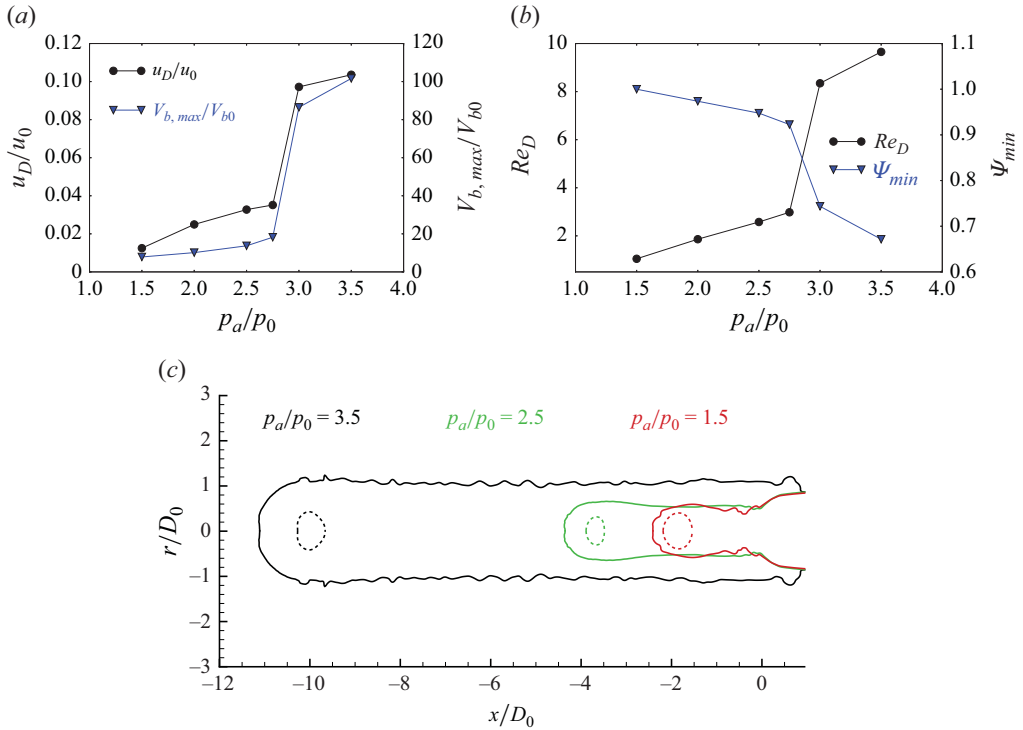
Figure 14. Dependence on driving pressure amplitude: (*a*) tunnel growth rate u_D and maximum bubble volume $V_{b,max}$; (*b*) Re_D and Ψ_{min}; and (*c*) the shape of the tunnel and the bubble are shown with the $\phi = 0$ (solid) and $\psi = 0$ (dashed) contours at $tu_0/D_0 = 108.4$.

behaviour, as reflected in the increase of Re_D for $p_a \leqslant 2.75p_0$ in figure 14(*b*). The sudden increase from $Re_D \approx 1$ to $Re_D \approx 10$ is similar to the threshold noted in other configurations (Freund 2008). This enables greater asymmetry during collapse as seen in figure 14(*c*). Both the increased expansion and asymmetry contribute to faster tunelling for $p_a \gtrsim 2.75p_0$.

Figure 15 shows that the primary effect of f is also via its impact on the bubble size. Frequencies lower than the natural bubble frequency f_n allow larger expansions, which here also cause more strain and damage, and faster and wider tunnelling (figure 15*c*). This also aligns with observations (Caskey *et al.* 2009*a*). The odd-looking non-monotonicity in the volumetric expansion $V_{b,max}$ is a consequence of being near resonance $f = f_n$. However, this is not sufficient to be consequential for the tunnelling: the dissipation in the system is sufficient that the tunnelling rate is essentially unaffected.

6. Effect of initial bubble location

Surprisingly, for many parameters considered, two different steady tunnelling solutions were found, depending on where the bubble was initialised. Results for different initial distances δx_{b0} of the bubble from the left end of the initial proto-tunnel in figure 2 are compared in figure 16(*a*). The calculations with the bubble further from the proto-tunnel end ($\delta x_{b0} \geqslant 0.625$) do not show jetting. After tunnelling is steady, the bubble initiated closer to the tunnel end ($\lesssim 0.9D_0$) is one-third the speed of the bubbles initiated further from the tunnel end ($\gtrsim 1.2D_0$): $u_D = 0.03u_0$ versus $u_D = 0.09u_0$, as shown in figure 16(*b*). This increase in the steady tunnelling rate correlates with the $V_{b,max}$ of the bubbles:
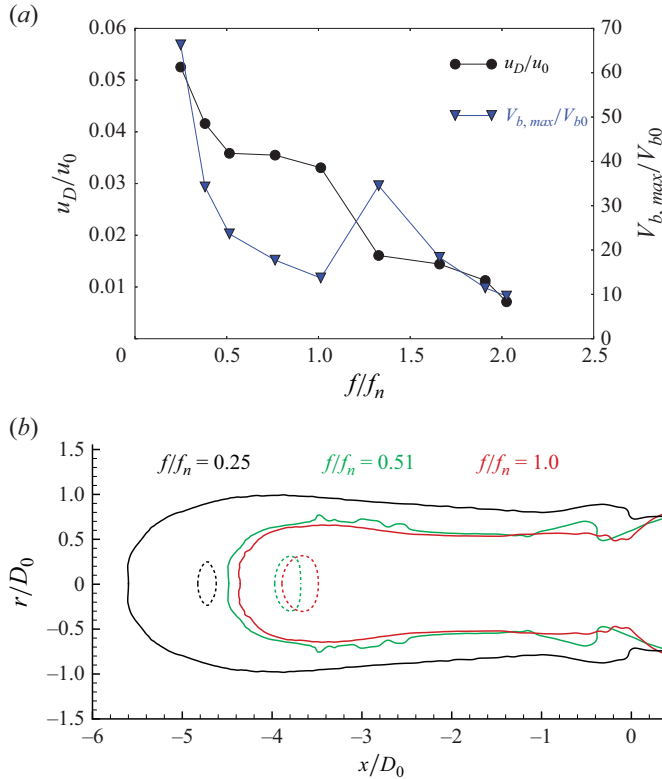
Figure 15. Dependence on excitation frequency f: (a) the tunnelling speed u_D and maximum volume $V_{b,max}$ and (b) the shape of the tunnel and the bubble are shown with the $\phi = 0$ (solid) and $\psi = 0$ (dashed) contours at $tu_0/D_0 \approx 105.4$.
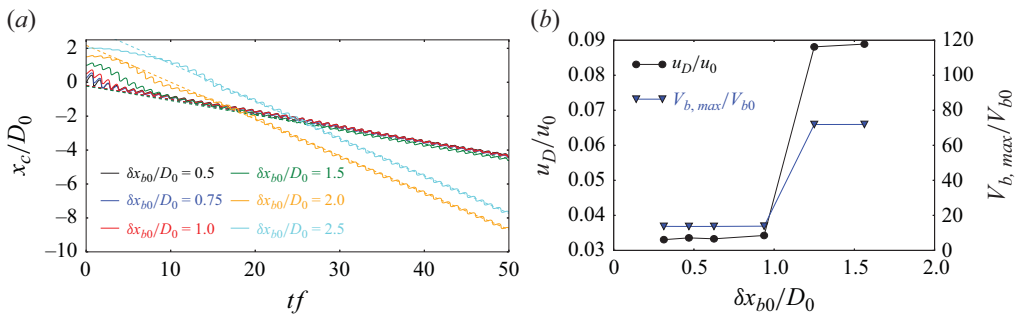

Figure 16. Effect of initial bubble distance from the tunnel end δx_{b0} on (a) tunnelling progress, and (b) speed and maximum bubble volume.

figure 16(b) shows that $V_{b,max} = 14V_{b0}$, for the cases where the bubble is initiated closer to the tunnel end, versus $V_{b,max} = 72V_{b0}$, when the bubble is initiated further away. Bubbles nearer the growing end of the tunnel are both more damaging and more asymmetric, which is necessary for translation, but they are also more confined. The bubbles further from the end can grow larger (and do), which promotes both damage and translation. Given this combination of factors, it is not surprising that two (or potentially more) steady tunnelling

conditions exist. However, no simple explanation for these two has been found given the complexity of the flow details.

7. Conclusions

The model introduced, which considers only viscous material and neglects elasticity due to the high frequencies, produces a microbubble tunnelling phenomenon similar to experiments. The tunnels in this model grow through a two-step process: strain causes damage in the expansion phase and the bubble moves towards the end of the tunnel during the collapse phase. Jetting collapse of the bubble is observed for some initial conditions only during the first few cycles of oscillation of the bubble, during which the jet rapidly damages the material at the tunnel end. However, the jetting ceases after a few cycles. The move-expand-stretch(-repeat) mechanism (§ 3) produces the steady tunnelling. Neither jetting nor acoustic radiation force (also neglected) is required.

The viscosity of the fluid, surface tension and degradation threshold influence tunnelling primarily via how they mediate the bubble expansion. There is a threshold material viscosity above which the tunnelling rate drops significantly. In this case, viscosity suppresses the large inertial expansion of the bubble, and the width and the growth rate both decrease. The bubble dynamics also depend on the excitation. Bubble expansion is greater for larger pressures and lower frequencies, both of which speed growth. The larger bubbles also leave wider tunnels. Ideally, many more simulations could be completed at still greater ranges of parameters to more completely map out parameters and examine scaling laws that might appear. Although these simulations are only two-dimensional, they require long time series, and thus do not yet provide conclusive scaling results across a wide range of parameters. We mostly focused on regimes where a mix of physical mechanisms (particularly viscosity and inertia) are both significant. Still more viscous simulations are more difficult due to time step stability limitations, and similarly higher inertia simulations require greater resolution and are more likely to precipitate three-dimensional effects.

It is important that such a simple model can produce tunnels, suggesting a potentially simple mechanism. However, the list of neglected components that might also play a role in experiments is long. Although the elasticity is not necessary for tunnelling, it will likely alter it, especially for stiffer materials. There is naturally no expectation of precisely matching the rates inferred from experiments, but they are not far from observations. For example, Acconcia *et al.* (2014) observed a microbubble translation rate of 0.5–6.8 cm s^{-1} in fibrin clots for ultrasound frequency 1 MHz and pressure 0.2–0.39 MPa. For water-like viscosity of the damaged material left in the tunnel, the simulated rates are somewhat faster, in the range of 6.8–69.6 cm s^{-1}, for similar acoustic excitation. However, this rate reduces by almost 85 % with a 10-fold increase in the viscosity of the degraded material. Viscosity well above that of water is expected due repolymerisation (Williams & Miller 2003) or just because degraded material will have significantly more molecularly complex components. Hence, the tunnelling rates here are not out of line with observations and expectations, providing additional validation, at least for the present purposes.

The axisymmetric model also does not support many instabilities that might lead to new bubbles and branching tunnels, which have been observed in certain cases (Williams & Miller 2003). It is possible that the axisymmetric constraint here plays the role of acoustic radiation in experiments in setting and maintaining the tunnelling direction. While our current model precludes azimuthal perturbation, these modes may affect dynamics. That stated, experiments (Prentice *et al.* 2005; Cattaneo *et al.* 2024) show that the bubbles are nearly axisymmetric when excited by lower pressure amplitudes. Further analysis will be

required to assess if the azimuthal shape modes will affect the tunnelling behaviour for the parameters considered, which is beyond the scope of our current work. It is interesting to speculate that non-axisymmetric instabilities cause bubble break-ups to the point where inertia balances viscosity such as in the regime considered here, which might produce tunnels as observed. We also consider only a case with a fixed gas volume, whereas in most applications, the bubble will include vapour formed by cavitation along with the non-condensible gases, which might introduce another time scale before achieving a steady behaviour. The thermodynamics of the gas and phase change might also alter the details of the response. Nevertheless, this simple model should guide efforts seeking either to increase material degradation (HIFU) or suppress it (BWL), improving therapies.

Declaration of interest. The authors report no conflict of interest.

REFERENCES

ACCONCIA, C., LEUNG, B.Y., MANJUNATH, A. & GOERTZ, D.E. 2014 Interactions between individual ultrasound-stimulated microbubbles and fibrin clots. *Ultrasound Med. Biol.* **40** (9), 2134–2150.

ACCONCIA, C., LEUNG, B.Y., MANJUNATH, A. & GOERTZ, D.E. 2015 The effect of short duration ultrasound pulses on the interaction between individual microbubbles and fibrin clots. *Ultrasound Med. Biol.* **41** (10), 2774–2782.

ARVANITIS, C.D., BAZAN-PEREGRINO, M., RIFAI, B., SEYMOUR, L.W. & COUSSIOS, C.C. 2011 Cavitation-enhanced extravasation for drug delivery. *Ultrasound Med. Biol.* **37** (11), 1838–1852.

BARAJAS, C. & JOHNSEN, E. 2017 The effects of heat and mass diffusion on freely oscillating bubbles in a viscoelastic, tissue-like medium. *J. Acoust. Soc. Am.* **141** (2), 908–918.

BARRANGOU, L.M., DAUBERT, C.R. & FOEGEDING, E.A. 2006 Textural properties of agarose gels. I. Rheological and fracture properties. *Food Hydrocolloid* **20** (2–3), 184–195.

CAIDEN, R., FEDKIW, R.P. & ANDERSON, C. 2001 A numerical method for two-phase flow consisting of separate compressible and incompressible regions. *J. Comput. Phys.* **166** (1), 1–27.

CALVISI, M.L., LINDAU, O., BLAKE, J.R. & SZERI, A.J. 2007 Shape stability and violent collapse of microbubbles in acoustic traveling waves. *Phys. Fluids* **19** (4), 047101.

CASKEY, C.F., QIN, S., DAYTON, P.A. & FERRARA, K.W. 2009*a* Microbubble tunneling in gel phantoms. *J. Acoust. Soc. Am.* **125** (5), EL183–EL189.

CASKEY, C.F., QIN, S. & FERRARA, K.W. 2009*b* Ultrasound mediated drug delivery: The effect of microbubbles on a gel boundary. *Annu. Intl Conf. IEEE Engng Med. Biol. Soc.* **2009**, 134–136.

CATTANEO, M., PRESSE, L., SHAKYA, G., RENGGLI, T., LUKIĆ, B., PRASANNA, A., MEYER, D.W., RACK, A. & SUPPONEN, O. 2024 Shape modes and jet formation on ultrasound-driven wall-attached bubbles. arXiv:2411.12371.

CHORIN, A.J. 1967 A numerical method for solving incompressible viscous flow problems. *J. Comput. Phys.* **2** (1), 12–26.

CURTISS, G.A., LEPPINEN, D.M., WANG, Q.X. & BLAKE, J.R. 2013 Ultrasonic cavitation near a tissue layer. *J. Fluid Mech.* **730**, 245–272.

FOLCH, R., CASADEMUNT, J., HERNÁNDEZ-MACHADO, A. & RAMÍREZ-PISCINA, L. 1999 Phase-field model for Hele-Shaw flows with arbitrary viscosity contrast. I. Theoretical approach. *Phys. Rev. E* **60** (2), 1724–1733.

FREUND, J.B. 2008 Suppression of shocked-bubble expansion due to tissue confinement with application to shock-wave lithotripsy. *J. Acoust. Soc. Am.* **123** (5), 2867–2874.

FREUND, J.B., SHUKLA, R.K. & EVAN, A.P. 2009 Shock-induced bubble jetting into a viscous fluid with application to tissue injury in shock-wave lithotripsy. *J. Acoust. Soc. Am.* **126** (5), 2746–2756.

GAUDRON, R., WARNEZ, M.T. & JOHNSEN, E. 2015 Bubble dynamics in a viscoelastic medium with nonlinear elasticity. *J. Fluid Mech.* **766**, 54–75.

GENT, A.N. & WANG, C. 1991 Fracture mechanics and cavitation in rubber-like solids. *J. Mater. Sci.* **26**, 3392–3395.

HAMAGUCHI, F. & ANDO, K. 2015 Linear oscillation of gas bubbles in a viscoelastic material under ultrasound irradiation. *Phys. Fluids* **27** (11), 113103.

HAN, B., KÖHLER, K., JUNGNICKEL, K., METTIN, R., LAUTERBORN, W. & VOGEL, A. 2015 Dynamics of laser-induced bubble pairs. *J. Fluid Mech.* **771**, 706–742.

HAN, R., ZHANG, A.M., TAN, S. & LI, S. 2022 Interaction of cavitation bubbles with the interface of two immiscible fluids on multiple time scales. *J. Fluid Mech.* **932**, A8.

HASAN, F., AL MAHMUD, K.-A.-H., KHAN, M.-I., PATIL, S., DENNIS, B.-H. & ADNAN, A. 2021 Cavitation induced damage in soft biomaterials. *Multiscale Sci. Engng* **3** (1), 67–87.

HUANG, J. & ZHANG, H. 2007 Level set method for numerical simulation of a cavitation bubble, its growth, collapse and rebound near a rigid wall. *Acta Mechanica Sin.* **23** (6), 645–653.

JIANG, G.S. & SHU, C.W. 1996 Efficient implementation of weighted ENO schemes. *J. Comput. Phys.* **126** (1), 202–228.

JOHNSEN, E. & COLONIUS, T. 2009 Numerical simulations of non-spherical bubble collapse. *J. Fluid Mech.* **629**, 231–262.

KAMRIN, K., RYCROFT, C.H. & NAVE, J.-C. 2012 Reference map technique for finite-strain elasticity and fluid–solid interaction. *J. Mech. Phys. Solids* **60** (11), 1952–1969.

KANG, M., FEDKIW, R.P. & LIU, X.-D. 2000 A boundary condition capturing method for multiphase incompressible flow. *J. Sci. Comput.* **15**, 323–360.

KIM, Y., WANG, T.Y., XU, Z. & CAIN, C.A. 2011 Lesion generation through ribs using histotripsy therapy without aberration correction. *IEEE Trans. Ultrason. Ferroelectr. Freq. Control* **58** (11), 2334–2343.

KING, L.V. 1934 On the acoustic radiation pressure on spheres. *Proc. R. Soc. Lond.* **147** (861), 212–240.

KLASEBOER, E. & KHOO, B.C. 2004 An oscillating bubble near an elastic material. *J. Appl. Phys.* **96** (10), 5808–5818.

KRISHNAN, S., HOPFINGER, E.J. & PUTHENVEETTIL, B.A. 2017 On the scaling of jetting from bubble collapse at a liquid surface. *J. Fluid Mech.* **822**, 791–812.

LANG, C., ADAMI, S. & ADAMS, N.A. 2024 Viscoelastic vapor bubble collapse near solid walls and corresponding shock wave formation. *Phys. Fluids* **36** (1), 013110.

LAUTERBORN, W. & OHL, C.-D. 1997 Cavitation bubble dynamics. *Ultrason. Sonochem.* **4** (2), 65–75.

LI, S.-M., ZHANG, A.-M., CUI, PU, LI, S. & LIU, Y.-L. 2023 Vertically neutral collapse of a pulsating bubble at the corner of a free surface and a rigid wall. *J. Fluid Mech.* **962**, A28.

LIU, C. & WALKINGTON, N.J. 2001 An Eulerian description of fluids containing visco-elastic particles. *Arch. Rat. Mech. Anal.* **159**, 229–252.

LUNDT, J.E., ALLEN, S.P., SHI, J., HALL, T.L., CAIN, C.A. & XU, Z. 2017 Non-invasive, rapid ablation of tissue volume using histotripsy. *Ultrasound Med. Biol.* **43** (12), 2834–2847.

MAXWELL, A.D., WANG, T.-Y., YUAN, L., DURYEA, A.P., XU, Z. & CAIN, C.A. 2010 A tissue phantom for visualization and measurement of ultrasound-induced cavitation damage. *Ultrasound Med. Biol.* **36** (12), 2132–2143.

MILNER, M.P. & HUTCHENS, S.B. 2021 Dynamic fracture of expanding cavities in nonlinear soft solids. *J. Appl. Mech.* **88** (8), 081008.

MOVAHED, P., KREIDER, W., MAXWELL, A.D., HUTCHENS, S.B. & FREUND, J.B. 2016 Cavitation-induced damage of soft materials by focused ultrasound bursts: a fracture-based bubble dynamics model. *J. Acoust. Soc. Am.* **140** (2), 1374–1386.

MURAKAMI, K., YAMAKAWA, Y., ZHAO, J.Y., JOHNSEN, E. & ANDO, K. 2021 Ultrasound-induced nonlinear oscillations of a spherical bubble in a gelatin gel. *J. Fluid Mech.* **924**, A38.

OHL, S.-W., KLASEBOER, E. & KHOO, B.C. 2015 Bubbles with shock waves and ultrasound: a review. *Interface Focus* **5** (5), 20150019.

ORTHABER, U. *et al.* 2020 Cavitation bubble collapse in a vicinity of a liquid-liquid interface – basic research into emulsification process. *Ultrason. Sonochem.* **68**, 105224.

PLESSET, M.S. 1949 The dynamics of cavitation bubbles. *J. Appl. Mech.* **16** (3), 277–282.

PLESSET, M.S. & CHAPMAN, R.B. 1971 Collapse of an initially spherical vapour cavity in the neighbourhood of a solid boundary. *J. Fluid Mech.* **47** (2), 283–290.

PLESSET, M.S. & PROSPERETTI, A. 1977 Bubble dynamics and cavitation. *Annu. Rev. Fluid Mech.* **9** (1), 145–185.

POPINET, S. & ZALESKI, S. 2002 Bubble collapse near a solid boundary: a numerical study of the influence of viscosity. *J. Fluid Mech.* **464**, 137–163.

PRENTICE, P., CUSCHIERI, A., DHOLAKIA, K., PRAUSNITZ, M. & CAMPBELL, P. 2005 Membrane disruption by optically controlled microbubble cavitation. *Nat. Phys.* **1** (2), 107–110.

PROSPERETTI, A. & LEZZI, A. 1986 Bubble dynamics in a compressible liquid. Part 1. First-order theory. *J. Fluid Mech.* **168**, 457–478.

RAYLEIGH, L. 1917 On the pressure developed in a liquid during the collapse of a spherical cavity. *Lond. Edin. Dublin Phil. Mag.* **34** (200), 94–98.

RODRIGUEZ, M., BEIG, S.A., BARBIER, C.N. & JOHNSEN, E. 2022 Dynamics of an inertially collapsing gas bubble between two parallel, rigid walls. *J. Fluid Mech.* **946**, A43.

SHANTHRAJ, P., SHARMA, L., SVENDSEN, B., ROTERS, F. & RAABE, D. 2016 A phase field model for damage in elasto-viscoplastic materials. *Comput. Meth. Appl. Mech. Engng* **312**, 167–185.

STRIDE, E. & COUSSIOS, C. 2019 Nucleation, mapping and control of cavitation for drug delivery. *Nat. Rev. Phys.* **1** (8), 495–509.

SUN, Y. & BECKERMANN, C. 2007 Sharp interface tracking using the phase-field equation. *J. Comput. Phys.* **220** (2), 626–653.

VLAISAVLJEVICH, E. *et al.* 2015 Effects of ultrasound frequency and tissue stiffness on the histotripsy intrinsic threshold for cavitation. *Ultrasound Med. Biol.* **41** (6), 1651–1667.

WANG, Q.X. & BLAKE, J.R. 2011 Non-spherical bubble dynamics in a compressible liquid. Part 2. Acoustic standing wave. *J. Fluid Mech.* **679**, 559–581.

WILLIAMS, A.R. & MILLER, D.L. 2003 The use of transparent aqueous gels for observing and recording cavitation activity produced by high intensity focused ultrasound. *IEEE Symp. Ultrason.* **2**, 1455–1458.

YAMAMOTO, T. & KOMAROV, S.V. 2020 Liquid jet directionality and droplet behavior during emulsification of two liquids due to acoustic cavitation. *Ultrason. Sonochem.* **62**, 104874.

YANG, X. & CHURCH, C.C. 2005 A model for the dynamics of gas bubbles in soft tissue. *J. Acoust. Soc. Am.* **118** (6), 3595–3606.

ZENG, Q., AN, H. & OHL, C.-D. 2022 Wall shear stress from jetting cavitation bubbles: influence of the stand-off distance and liquid viscosity. *J. Fluid Mech.* **932**, A14.

ZHANG, W. *et al.* 2019 AMReX: a framework for block-structured adaptive mesh refinement. *J. Open Sour. Softw.* **4** (37), 1370.